An x-ray tomography facility for quantitative prediction of mechanical and transport properties in geological, biological and synthetic systems.

Arthur Sakellariou[a], Tim J. Senden[a], Tim J. Sawkins[a], Mark A. Knackstedt[a], Michael L. Turner[a], Anthony C. Jones[a], Mohammad Saadatfar[a], Ray J. Roberts[a], Ajay Limaye[b], Christoph H. Arns[a], Adrian P. Sheppard[a] and Rob M. Sok[a]

[a] Department of Applied Mathematics, Research School of Physical Sciences and Engineering, The Australian National University, Canberra ACT 0200, Australia;

[b] VizLab, Supercomputing Facility, The Australian National University, Canberra ACT 0200, Australia

ABSTRACT

A fully integrated X-ray tomography facility with the ability to generate tomograms with 2048^3 voxels at 2 micron spatial resolution was built to satisfy the requirements of a virtual materials testing laboratory. The instrument comprises of a continuously pumped micro-focus X-ray gun, a milli-degree rotation stage and a high resolution and large field X-ray camera, configured in a cone beam geometry with a circular trajectory. The purpose of this facility is to routinely analyse and investigate real world biological, geological and synthetic materials at a scale in which the traditional domains of physics, chemistry, biology and geology merge. During the first 2 years of operation, approximately 4 Terabytes of data have been collected, processed and analysed, both as static and in some cases as composite dynamic data sets. This incorporates over 300 tomograms with 1024^3 voxels and 50 tomograms with 2048^3 voxels for a wide range of research fields. Specimens analysed include sedimentary rocks, soils, bone, soft tissue, ceramics, fibre-reinforced composites, foams, wood, paper, fossils, sphere packs, bio-morphs and small animals. In this paper, the flexibility of the facility is highlighted with some prime examples.

Keywords: X-ray micro-tomography, mesoscale physics, porous media, transport and mechanical properties

1. INTRODUCTION

For many years, this department has been active in the fields of intermolecular forces, surface chemistry, surface physics and molecular self-assembly at the nano-scale. The properties at this scale play an important part in understanding the physical and transport properties of materials at larger scales, especially the relationships with topology and surface form. This work has evolved more recently up to the mesoscale. At this scale, the traditional domains of physics, chemistry, biology and geology merge. To experimentally investigate this scale, a purpose built X-ray tomography facility was commissioned to investigate all media, be it porous, disordered or complex.

In section 2, the tomography facility and its capabilities are described. Once the volume data of a specimen have been generated, there are many techniques available for qualitative and quantitative analysis. In section 3, the analysis techniques commonly used in our department are outlined, including the primary steps of visualisation and segmentation. In section 4, a number of our key applications are outlined. By far our most intensive application is the analysis of transport and elastic properties of porous media, mainly in the context of calculating physical properties of oil bearing rocks, and recently, for ground water studies. Other applications described in

---

Further author information: (Send correspondence to A. Sakellariou)
A. Sakellariou: E-mail: arthur.sakellariou@anu.edu.au, Telephone: 61 (0)2 6125 4975
T.J. Senden: E-mail: tim.senden@anu.edu.au, Telephone: 61 (0)2 6125 4781
M.A. Knackstedt: E-mail: mark.knackstedt@anu.edu.au, Telephone: 61 (0)2 6125 3357

Developments in X-Ray Tomography IV, edited by Ulrich Bonse, Proc. of SPIE Vol. 5535
(SPIE, Bellingham, WA, 2004) · 0277-786X/04/$15 · doi: 10.1117/12.559200

this section include the analysis of bone regeneration in scaffold implants, mechanical and thermal properties of polymeric foams, characterisation of granular material and the imaging of multi-phase fluid saturation and fluid penetration in paper.

2. THE FACILITY

Tomography is a technique that generates a data set, called a *tomogram*, which is a three dimensional representation of the structure and variation of composition within a specimen. Each three dimensional point in the tomogram is called a *voxel*. At this facility, X-rays from a micro-focus X-ray source are used to probe the specimen and an X-ray camera is used to record the X-ray transmission radiograph. To generate the tomogram, a series of radiographs are collected at different viewing angles by rotating the specimen. This set of radiographs, called *projection* data, are processed with a reconstruction algorithm to generate the tomogram of the specimen. For more details about X-ray tomography, see.[1, 2]

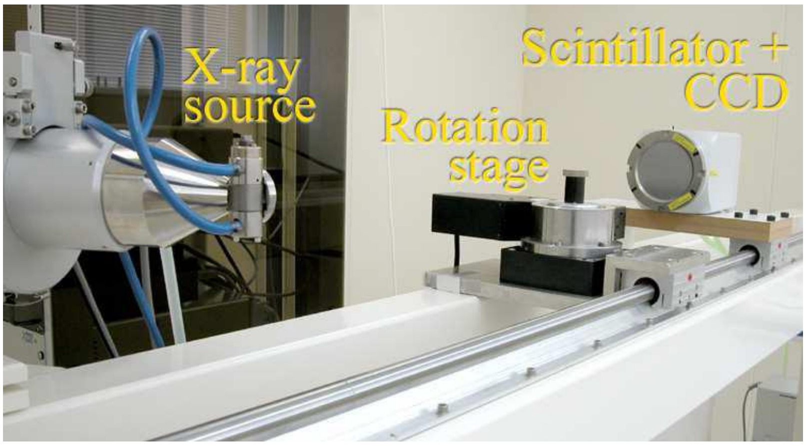

Figure 1. A photo of the X-ray tomography instrument.

The instrument at this facility is shown in Figure 1. It consists of three main components: the X-ray source, the rotation stage and the X-ray camera. The X-ray source is an X-Tek RTR-UF225 which generates polychromatic X-rays using a 30–225 kV / 1mA electron beam with 2–5 µm spot size. The rotation stage is a Newport RV120PP with a 1 milli-degree accuracy and is capable of supporting 120 kg. The X-ray Camera is a Roper PI-SCX100:2048 with an active area of 70 × 70 mm^2 and 2048 × 2048 16-bit pixels. Additionally, a shutter (not shown) made from a 2.5 mm thick piece of platinum prevents excessive exposure of the X-ray camera during image download. Both the rotation stage and the X-ray camera can be translated to obtain magnifications between ×1.1 to over ×100. This allows the large field (60 mm cross-section with 30 µm voxel size) or high resolution (4 mm cross-section with 2 µm voxel size) aspect of the instrument to be exploited. To explore various contrast enhancing techniques, the rotation stage has a large aperture and sufficient clearance underneath to attach various experimental apparatus, such as mechanical and fluid pumps, allowing the entire experimental apparatus to rotate with the specimen. For more details about this instrument, see.[3, 4]

At present, there are two minor limitations with this system. The first is polychromatic X-rays result in the phenomenon of beam hardening, which introduces artifacts in the tomogram. This effect is minimised by pre-filtering the X-ray beam. Typically, the filter is chosen to have the same composition as the major constituent in the specimen and with a thickness about 25–50% the diameter of the specimen. The second is that a circular trajectory with a cone beam geometry can only generate accurate tomograms if Tuy's sufficiency condition[5] is satisfied. Problems predominate if specimens consist of a periodic distribution of parallel planar edges, in which the normals of these edges are aligned parallel to the rotation axis. Fortunately, in the analysis of porous, disordered and complex media, specimens typically do not have such structures so this limitation does not pose a serious problem. To reduce the significance of this limitation, the camera length is typically set to 2500 mm, which results in a cone angle of only 0.8°. Even with these limitations, very high quality and accurate tomograms are generated with this instrument.

Specimens are analysed by collecting projection data. Because of the cone beam geometry, the specimen is rotated through 360°. To generate a 1024^3 voxel tomogram, 1600 projections are collected over 3–28 hours, resulting in approximately 3 GBytes of projection data. To generate a 2048^3 voxel tomogram, 3000 projections are collected over 15–48 hours, resulting in approximately 24 GBytes of projection data. The range in the data collection times depend on the amount of beam filtering used. The reduction of beam hardening artifacts more than compensates for the inconvenience of increased collection times. To generate a tomogram, the projection data are pre-processed. This consists of linearising the data, followed by steps that minimise artifacts in the tomogram that are the result of non-ideal aspects of the experiment. The most common are the result of cosmic rays, defects, non-linear sensitivity and spatial non-linearity in the X-ray camera, misaligned cone beam geometry and specimen rotation and variability of the X-ray flux from the source.[3] Once the projection data are pre-processed, they are reconstructed using a modified Feldkamp algorithm.[6] All data are processed at the Australian Partnership for Advanced Computing (APAC) national facility,[7] which houses a Compaq AlphaServer super-computer. It takes 40–50 minutes on 32 CPUs to generate a 1024^3 voxel tomogram and 200–300 minutes on 128 CPUs to generate a 2048^3 voxel tomogram.

3. SOME ANALYSIS TECHNIQUES

Once a specimen has been imaged, the tomogram can be analysed to measure a range of parameters and properties that relate to the specimen. A number of quantitative techniques have been developed in-house to analyse tomograms, including the two major steps of visualisation and segmentation. One important feature of all our implementations is that the software is written to run on cluster-type parallel computers, thus allowing all simulations and calculations to be performed in three dimensions, not just on selected two dimensional cross-sections.

3.1. Visualisation

2D Imaging: The first step in analysing a tomogram is to image cross-sections. Software is available to set the orientation of a cross-section and to sweep it through the tomogram or a sub-volume of the tomogram. By setting the contrast of the 2D image, various features can be identified. Ultimately 3D imaging should give the best view of the structure in a tomogram but sometimes the 3D information is too dense for easy interpretation. In this case, sweeping a cross-section through the tomogram provides the best method to image the 3D structure by allowing one to build up a mental image.

3D Imaging: Volume rendering is a 3D imaging method wherein features in a data volume are rendered directly without decomposing it into geometric primitives. The density within a tomogram is assigned a colour and transparency that depend on lookup tables which are set by the user so that particular features or regions of uniform density in the volume can be imaged. A 3D image of the tomogram is generated, at viewing angles (θ, ϕ), by tracing rays through the tomogram. Each ray is attenuated and coloured depending on the transparency of its route through the tomogram and finally sets the colour of a pixel in the image. A 2GHz Pentium 4 with 1 Gbyte of RAM is used to generate one image in about a minute, using custom written C++ code. Examples of single frames are shown in section 4. In many cases, it is difficult to interpret complex 3D structure in a static 3D image so typically, movies are generated. A series of 3D images are rendered for a range of viewing angles, including trajectories through the volume, and are collated into either the mpeg or avi format. Examples of movies are available at: "http://wwwrsphysse.anu.edu.au/appmaths/ct_movies".

3.2. Segmentation

Images of porous and composite materials are composed of different regions, each with a comparatively uniform density or with zero density for the pore space. These different regions, called *phases*, reflect the different substances present within the material. In order to compute the morphological and physical properties of the material, one must identify these phases, thereby partitioning the grey-scale image into disjoint segments. To do this, one must decide to which phase each voxel belongs. This process is called segmentation.

We have developed a new, multi-stage procedure that combines novel and traditional algorithms for the segmentation of porous or composite materials.[8] Segmenting such tomograms is a particular challenge because there are often features at or below the instrument resolution which blur the sharp edges at phase boundaries. As a consequence, significant features can be lost and macroscopic properties of the segmented image can vary greatly with small changes in the segmentation parameters. No solution can claim to be perfect. Our algorithm involves a three-stage approach: The first stage is an anisotropic diffusion filter[9] which removes noise while preserving significant features. The second stage applies the unsharp mask sharpening filter[10] which enhances edges and partially reverses the smoothing that is often a consequence of tomographic reconstruction.

Finally, the segmentation itself is performed using a combination of watershed[11] and active contour methods.[12] We have achieved high efficiency by developing a parallel version of the fast marching method[13] using a time-warp, or parallel discrete event simulation,[14] approach. This algorithm has been shown to scale well to hundreds of CPUs on cluster-type parallel computers, and applied to cubic images comprising up to 2048^3 voxels.

3.3. Summary of Quantitative Analysis Techniques

A segmented tomogram is already naturally discretised and lends itself immediately to numerical computation of a number of properties. In this section, the techniques which are well established and are applied on a regular basis are outlined.

Phase Fraction and Surface-to-volume: These are directly evaluated by simply counting the numbers of voxels and faces in the tomogram.[15]

Topology: The topology or connectivity of a phase is characterised by its skeleton, which is the volume of the phase represented by a three-dimensional line graph.[16, 17]

Pore Network Model: Simplification of the complex 3D morphology of a pore space as a interconnected network of large porous bodies (pores) connected by smaller constrictions (throats). The vertices of the skeleton are used to determine pore body sizes, and the throats defined by the minimal constriction between pore bodies[16, 17]

Capillary Pressure and Pore size distribution: The pore size of a 3D image is based on defining locally for every point within the structure the diameter of the largest sphere within the pore phase.[18, 19] Drainage capillary pressure is simulated using a similar technique.

Diffusion: To predict the diffusion of a fluid residing in a void phase, the Brownian motion of a diffusing particle is simulated using a random walk algorithm.[20]

Conductivity: The voxelated grid is converted into a network of resistors by placing a resistor at every voxel. The resistivity of each voxel is defined by the phase. The Laplace equation is solved by applying a potential gradient to each coordinate direction and the system is relaxed using a conjugate gradient technique to evaluate the field.[21]

Permeability: The lattice-Boltzmann method[22–24] is used because it is a mesoscopic approach to computational fluid dynamics and has found much success in fluid-flow applications of porous media. It is simple in form, can be adapted to complex flow geometries and can incorporate complex fluid/solid, fluid/gas and fluid/fluid interfaces.

Elastic Properties: A finite element method is used to estimate the elastic properties of the tomogram. Each voxel is taken to be a tri-linear finite element. The solver minimises the elastic energy via a conjugate gradient method.[25–28]

3.4. Simulations on Sub-volumes

To perform a numerical simulation on a single tomogram made up of billions of voxels requires substantial computing resources. For example, to calculate the fluid permeability, a simulation on a 1024^3 voxel tomogram would require 256 GBytes of memory and over 5,000 CPU hours. On a 2048^3 voxel tomogram, it would require 2 TeraBytes of memory and over 40,000 CPU hours. Previous research has shown[21, 24, 28, 29, 33] that accurate predictions can be made on sub-volumes. The size of the sub-volume must be large compared to some statistical length scale (e.g., correlation length, mean grain/pore size). Therefore, a compromise between too few voxels, which leads to errors in a simulation, and maximising the volume size, such that computation is feasible, is necessary. An added benefit of using multiple sub-volumes is the ability to generate a range of independent measurements from a single tomogram, instead of only one. If the porosity (fraction of voxels in the pore/void phase) varies throughout the tomogram, different sub-volumes will result in different measurements and a distribution can be generated with respect to porosity.

4. SOME APPLICATIONS

While there is increasing international recognition that the rapid growth of high-resolution 3D imaging technology can impact on the interpretation of complex material properties there is generally a lack of the parallel development in computational modelling of physical properties of complex materials. This development is essential to the harnessing of the full potential of 3D imaging methods. In this section we describe applications of quantitative imaging to a range of disciplines.

4.1. Petrophysical and Hydrodynamic Properties of Sedimentary Rock

Hydrocarbon recovery from reservoir rocks and contaminant dispersion in soils are currently estimated on the basis of laboratory scale measurements and are then applied to the field scale, without explicit consideration of the effects that rock microstructure and rock-fluid interactions have on the scaling behaviour of these measurements. The ability to image pore structure and fluid distributions within rocks and soils has the potential to significantly improve hydrocarbon recovery and produce more effective ground water remediation strategies. To date, more than 150 tomograms of granular packs, sedimentary rocks and soil specimens have been collected at our facility. Numerical predictions of a range of important physical properties (e.g., conductivity, diffusivity, fluid permeability, multiphase flow and elastic properties) have been simulated directly on these tomograms.

We illustrate this for a suite of Fontainebleau sandstone samples displaying a wide range of porosities. The conductivity, elasticity and fluid permeability have been derived numerically from tomograms. As an example, figure 2a shows the calculated permeability compared with laboratory measurements. Predictions from the simulations are in excellent agreement with laboratory measurements across four *orders of magnitude* in permeability. This result illustrates the feasibility of combining microtomographic images with numerical calculations to accurately predict properties of complex porous materials. Recently, this methodology has been applied to a range of petroleum reservoir rocks with excellent results.[30–36] In figure 2b, two cross-sections of sandstone tomograms are shown to demonstrate the clarity of the data collected at this facility.

4.2. Health and Physical Properties of Bone and Related Biomaterials.

The ability to examine bone structure at high resolutions, and in three dimensions, is of immense interest in predicting bone health and fracture risk. Application of micro-CT to image and analyse bone micro-architecture has previously been demonstrated by Ruegsegger,[37] Ritman,[38] and Kinney,[39] and has resulted in the development of a range of 3D bone morphology measures. Micro-CT data has also been used to generate finite element models to solve for local stresses and strains within bone.[40–42]

At our facility, the structural, elastic and transport properties of various bone systems are being investigated. This includes the structure and porosity of cortical bone[43, 44] and of newly mineralised bone within tissue engineered scaffolds.[44, 45] Estimations of elastic properties have been made on the mineralising tissue, which indicate a partial recovery, within the scaffold, of a full load bearing capacity at three months post implant. Two other areas of promise include the estimation of stress fields in *ex situ* osteoporotic human femoral necks and rat vertebrae. The local stress fields may indicate regions where bone failure is likely to initiate and will be correlated with *in situ* compression imaging.

We illustrate our work with two examples. The first example is the regeneration of bone tissue within a polymer scaffold. A 2x2x3mm piece of regenerated bone and scaffold was imaged at a voxel size of 1.6 µm to generate an image of 2048^3 voxels. Figure 3a is a volume rendering of the full tomogram, binned down to a 512^3 voxel data set. The scaffold has been removed for clarity but is present in the large cylindrical voids. The pore space within the regenerated bone is well connected and may provide insights into the transport properties of neovascular (newly formed) channels, which would contain blood vessels and larger cells. The second example involves the analysis of Haversian and Volkmann canals within human cortical bone. A piece of bone, measuring 1x1x2mm

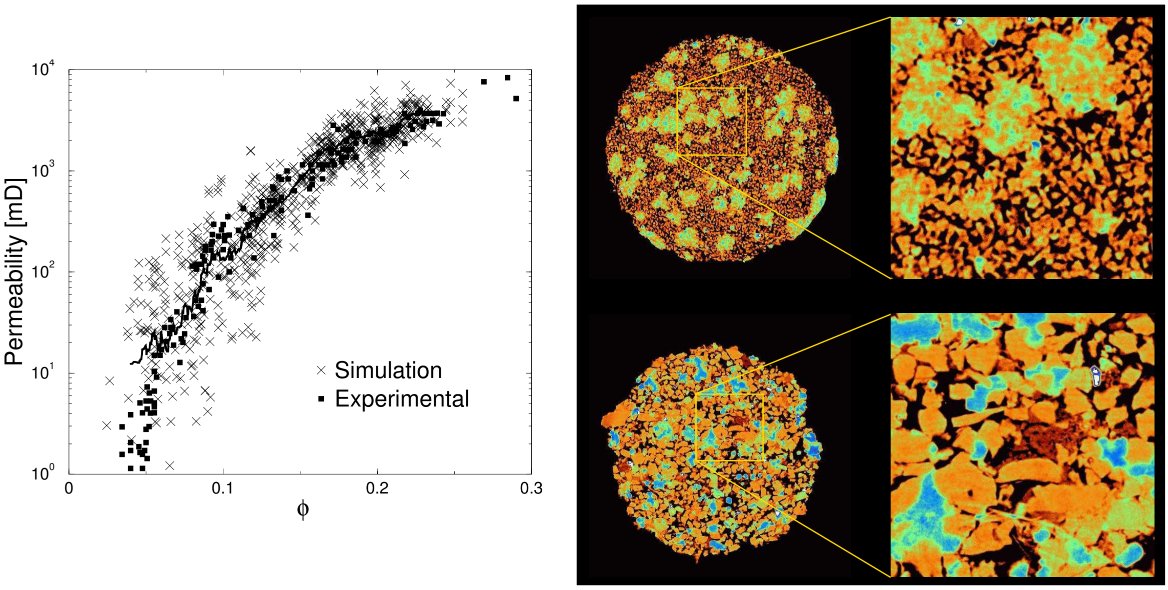

a) Permeability vs. Porosity b) Examples of sandstone

Figure 2. a) Comparison of simulated permeability on tomograms with experimental data as a function of porosity. The solid line gives the averaged data over all simulation data. Excellent agreement is found over 4 orders of magnitude in permeability. Note that the simulated data came from 4 tomograms whereas over 50 specimens were required for the experimental data. b) Two 2048^2 pixel cross-sections from sandstone tomograms. The top sandstone was imaged at a voxel size of 2.6 µm and the bottom imaged at 5.2 µm. The zoomed region comprise of 512^2 pixels and highlight the full imaging potential of the facility. The density varies from low to high as black, red, orange, yellow, green and blue.

long, was taken from the mid-diaphysis of a human femur and was imaged at 0.8 µm to produce a 2048^3 image. Figure 3b is a volume rendering of the full tomogram, again binned down to a 512^3 voxel data set. Various structural and physical properties of the Haversian network can be estimated directly from the tomographic data, which can provide insight into the changes in bone strength brought about by bone remodelling.

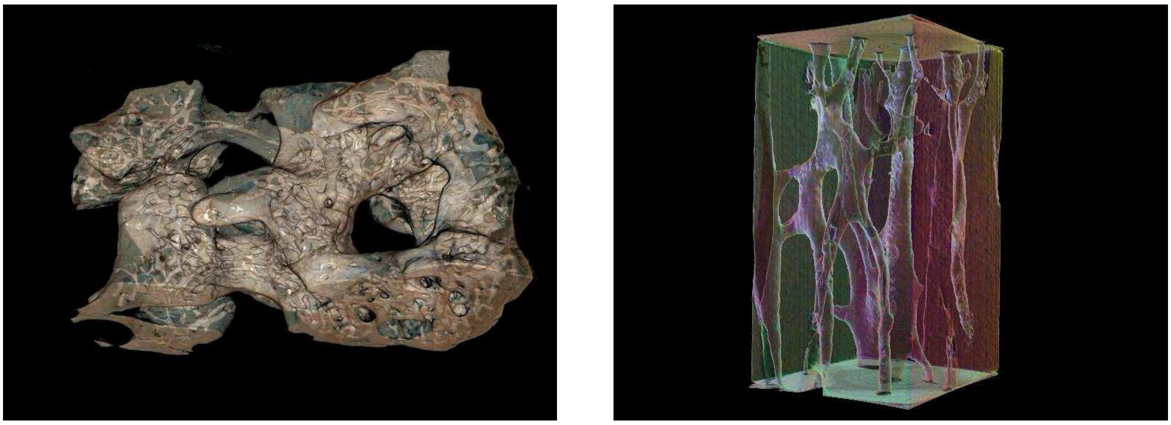

a) Regenerated Bone b) Cortical Bone

Figure 3. Volume renderings of two types of bone. a) Regenerated bone within a polymer scaffold (transparent). b) Human cortical bone.

4.3. Polymeric Foams

Properties of a range of engineered materials including foamed solids are a direct consequence of their microstructure. To improve these materials it is necessary to understand exactly how the microstructure determines these properties. Imaging these materials in 3D is enabling researchers to accurately describe the complex structure and to simulate the mechanical and transport properties of these materials.

We illustrate this for a suite of closed-cell polymeric foamed materials with a range of porosities. The density of the polymer matrix was $\simeq$ 1200 kg/m^3 and the foam densities ranged from 350 kg/m^3 to 650 kg/m^3. The pores within the foam structures were generally spherical. The foams were cut into samples $\approx$ 4 mm squared and $\approx$ 10 mm in length and imaged at 1024^3 voxels and a voxel size of 6.7 µm. Figure 4a shows a collection of 3D volume renderings of 3 typical cases of foam structure. The thermal conductivity and elasticity have been calculated,[46] and by way of example, figure 4b shows the gas permeability as a function of the porosity. Each tomogram was sub-sampled to a size of 200^3 voxels, allowing approximately 20 independent data points from each tomogram. The variation in permeability is observed over 5 orders of magnitude.

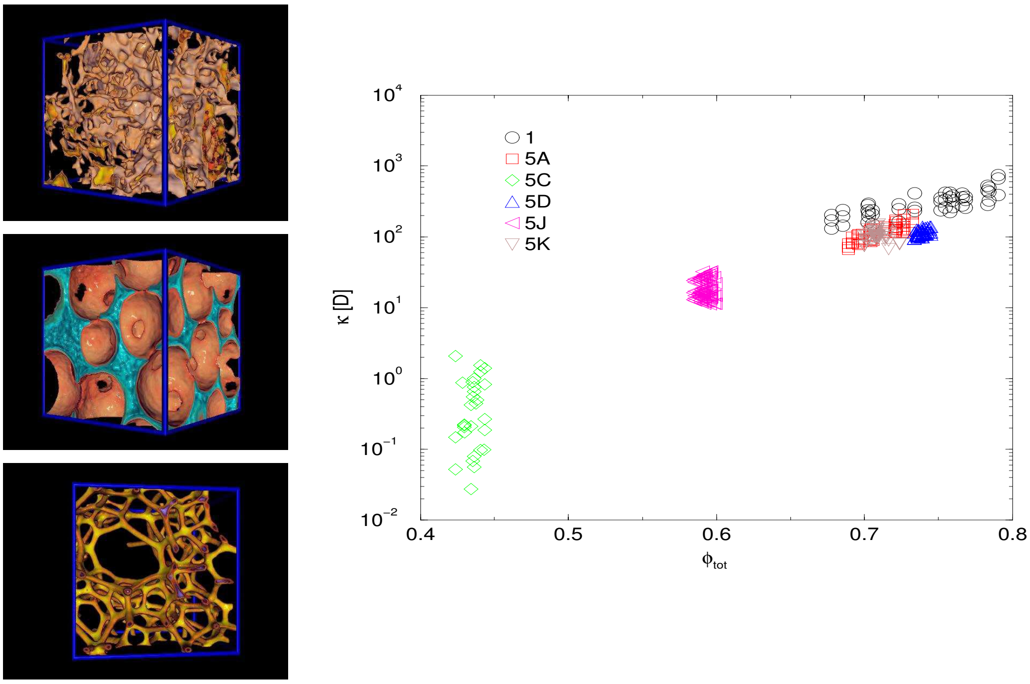

a) Various 1x1x1mm foam subsets

b) Gas permeability vs. Porosity.

Figure 4. a) Volume renderings of three foam classes. b) Gas permeability of 6 industrial foamed materials as a function of the porosity. The variation in permeability is observed over 5 orders of magnitude.

4.4. Granular material

The science of granular materials has a long history. In the last few years there has been a resurgence of interest in this field. Indeed, much engineering literature is devoted to understanding how to deal with these materials. Nevertheless, the technology for handling and controlling granular materials is not as well developed as that for handling other systems such as conventional fluids. Estimates suggest that we waste 40% of the capacity of many industrial plants because of problems encountered in dealing with these materials.[47,48] Sandpiles, vibrating grains and sphere packings are presently the research subject of many scientists around the world.[47,49–51] Some of the current key topics can be subdivided in two main categories – *static*: geometrical structure, limiting densities, stress propagation and mechanical behaviour, and *dynamic*: slow dynamics during compaction, size segregation, critical slowdown, jamming and glass-transition, disorder-order transition and crystallisation. Many of these topics can only be resolved with accurate and large scale 3D investigation. X-ray tomography can now provide datasets[52] with a number of particles which rival numerical simulation.

Although tomography gives the ideal opportunity to investigate grain configurations, there are several deficiencies inherent in the technique. Firstly, rapid dynamic events are lost in the time required to acquire a tomographic sequence. Secondly, finite resolution introduces ambiguity in identifying grain contacts, which can severely limit statistical or topological descriptions of the grain pack. At our facility, some approaches to reduce these limitations have been implemented. One approach is to rely on simple, rapid radiography of the pack in motion to directly capture 2D density fluctuations. Grain displacement maps can be made by comparing tomograms before and after an event, and allow the radiographs to be calibrated. Figure 5a illustrates a differential transverse section through a rubber bead pack before and during a compression. The definition of the actual grain contact network can, for some systems, be elucidated by the condensation of an X-ray opaque liquid into the pore space. Provided sufficiently stable temperature can be maintained, the presence of a condensate identifies that two adjacent grains are within a few 100 nm of each other, thus indirectly going below the limiting resolution of the X-ray source. Figures 5b and 5c show equilibrium condensation between spheres and irregular grains, respectively.

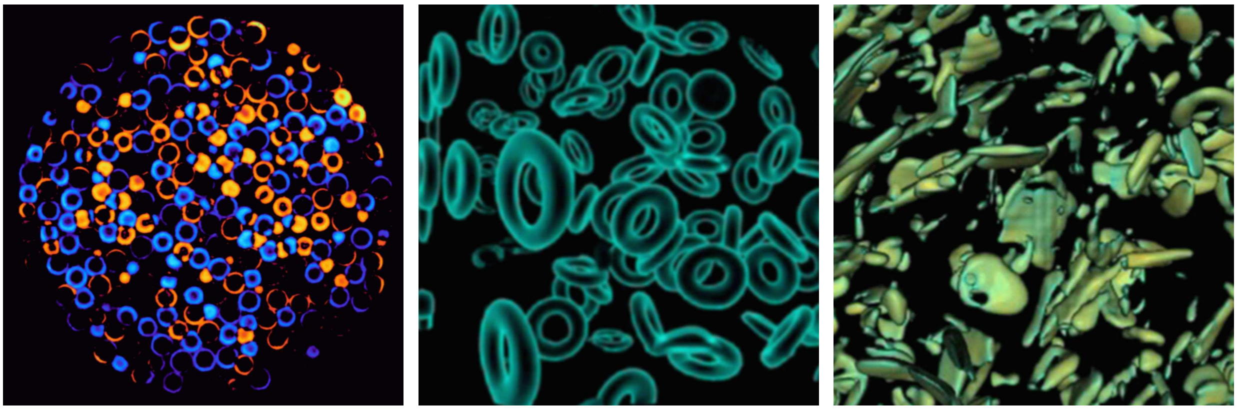

a) Rubber bead compression

b) Condensation between spheres

c) Condensation between irregular grains

Figure 5. a) A transverse section through a pack comprising 3.2 mm rubber beads made by subtracting the tomograms before and during static loading. Blue denotes a bead has been displaced in the same direction as loading, orange denotes a counter displacement. b) A micro-litre subset of a dataset showing condensates formed between touching 1-2 mm beads. The beads have been rendered transparent to show the annular condensates only. Note that due to finite resolution the true cross-section of the menisci is lost, however the presence of the condensates indicates the beads are in very close proximity: <100 nm. c) A similar illustration as figure 5b except the grains are now irregular shards permitting a larger range of contact geometries. The annular rings are now rare and sheet structures dominate.

4.5. Imaging of Multi-phase Saturation.

Mapping the distribution of multiple fluid phases within a porous rock or soil is crucial to understanding mass transfer in contamination and remediation of ground water and in the prediction of hydrocarbon reserves. The experimental procedure involves encasing a specimen, with the top and bottom surfaces connected to a reservoir of fluid with a mechanism to adjust the pressure. A tomogram of the specimen with pressure applied to the fluid reservoir typically lacks sufficient contrast to image the fluid. To increase this contrast, it is possible to dope the fluid with a high contrast medium. Alternatively, a tomogram is collected of the dry specimen and another of the fluid saturated specimen. By calculating the difference of these two tomograms, a 3D map of the fluid saturation is imaged. After segmentation, the fractional fluid saturation is calculated by counting the fluid saturated voxels that are connected to the reservoir. The tomographic mapping of fluid distribution in porous media requires a spatially stable test cell. Small specimen displacements between successive tomograms can be computationally tedious to realign. One of the benefits in designing a stage mount with high rigidity and strength is that very small variations in voxel opacity can be mapped by difference.

In one study,[54] an experiment was performed on a 8 mm sandstone core, which had it's edges encased in resin and was imaged at 1024^3 voxels and a voxel size of 9 µm. Firstly, it was imaged dry, then saturated under vacuum with a fluorocarbon (3M Flourinet, surface tension $\sigma = 16$ dynes/cm) and after free drainage was imaged again. The difference map was segmented to identify the residual wetting phase saturation, as shown in figure 6a. Analysis of the tomogram shows the wetting phase saturation at 60%. In figure 6b, a 3D volume rendering of the phase distribution is shown for a small 128^3 voxel sub-volume. The presence of the wetting phase in the smaller pore spaces and along much of the pore/grain interface is observed and is consistent with previous observations.[55] Examples of accurate single phase absolute permeability calculations are shown in figure 2a. This is extended to calculate the effective relative permeability of the non-wetting phase. These computations were performed on four (300^3) sub-tomograms. In figure 6c, the results are compared to laboratory measured data[56] and are in good agreement.

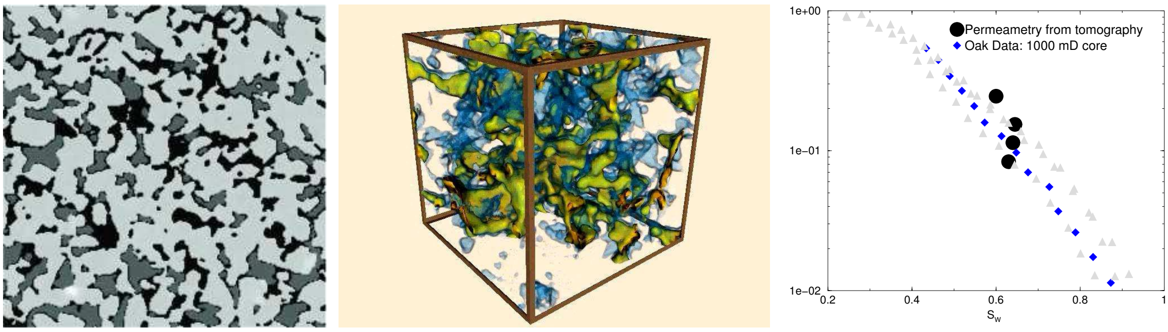

a) Fluid configuration in 2x2mm cross−section

b) Fluid configuration in 1x1x1mm volume

c) Relative Permeability vs. Saturation

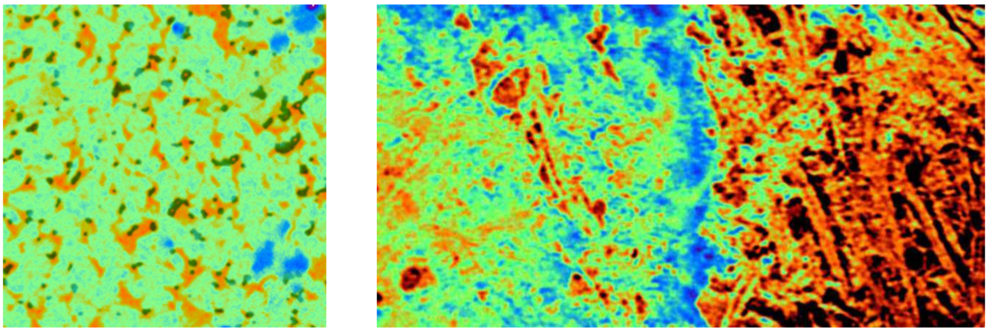

d) Clay typing

e) Fluid penetration into paper

Figure 6. a) A cross-section of the experimental two phase fluid configuration during drainage in sandstone at 60% wetting phase saturation. The dark phase gives the residual wetting phase, the non-wetting phase is dark grey and the grains are the lightest shade. b) A sub-tomogram shows the wetting phase (dark/blue) and the non-wetting phase (light/green) within a subsection of the core (grains removed). c) The graph shows the computed relative permeability measured on subsets at $(1.5mm)^3$ and comparison with experiment. d) A 1 mm^2 sub-set of a cross-section through a permeable, clay-bearing sandstone. The section is a difference of two consecutive tomograms obtained by first imaging the rock dry, followed by Cs-labelling of the clay from solution, and finally imaging the subsequently drained rock core. The Cs-labelled regions appear as dark green regions and overlay the orange coloured pore space. e) A coronal section through the mid-plane of an unsized paper sheet showing a snap frozen fluid imbibing (left to right). The fluid is seen as green to blue, with voids as dark to black, and fibres as orange. Note the voids shown do not connect with either surface of the sheet and represent trapped air. This sub-set is approximately 800 µm wide.

The delineation of the clay distribution in rocks benefits from the approach used to map fluids. One of the drawbacks of using a conventional X-ray source is that clay, feldspar and other minerals have indistinguishable attenuations and cannot be identified unambiguously. The presence of clays has an important effect on fluid transport and other petrophysical properties (resistivity, NMR response, elasticity) of sedimentary rocks. To enhance our understanding of the role of clays in rocks, one must map the spatial distribution of clays. In figure 6d, an attempt was made to ion exchange the natural sodium ion with the more X-ray opaque caesium ion.[53] Although the procedure was verified on a cut section with electron microscopy, the signal-to-noise is poor. The technique would benefit from acquiring multiple exposures to improve signal quality. Care must be taken with the ionic strength of the solutions to prevent adverse swelling of the clays.

Many of the principles of fluid penetration found in rocks extends naturally into other porous materials. Figure 6e shows a wetting fluid, snap frozen as it imbibes into paper. In paper, as in rocks, the primary mechanism of flow is via films which track along the channels formed between fibre overlaps.[57] This is a contrary view to the accepted model in which it is the voids between fibres which conduct the fluid, in an analogous way to tortuous capillaries.[58, 59] Although paper presents many difficulties for reliable tomographic imaging using conventional X-ray sources, the mapping of saturation profiles is fruitful and helps to quantify paper performance directly.

5. DISCUSSION

We have aimed to illustrate that an integrated tomography facility relies crucially on a substantial investment in quantitative 3D analysis. While commercial tomography instruments are increasingly popular, their capacity to realise physical properties from data sets is currently very restrictive. The reliance on speciality code and a substantial computer resource is most likely the source of this limitation. In addition, many fundamental issues of dealing with discretised three-dimensional data remain open research topics.

ACKNOWLEDGMENTS

The authors gratefully acknowledge fruitful discussions with Val Pinczewski, Bruce Milthorpe, Stephen Hyde and Tomaso Aste. The authors thank the Australian Research Council (ARC) for support of the hardware development and Australian Partnership for Advanced Computing for funding and generous access to supercomputing resources. The Cooperative Research Centre for Functional Communication Surfaces is also gratefully acknowledged for financial support. Turner thanks for support from the Cooperative Research Centre for Landscape Environments and Mineral Exploration. Senden gratefully acknowledges the ARC for his fellowship.

REFERENCES

1. AC Kak, M Slaney, *Principles of Computerized Tomographic Imaging*, IEEE Press, 1988.
2. CA Carlsson, *Imaging Modalities in X-ray Computerised Tomography and in Selected Volume Tomography*, Phys. Med. Biol. **44** R23-56, 1999.
3. A Sakellariou, TJ Sawkins, TJ Senden, Internal ANU Document, in preparation.
4. A Sakellariou, TJ Sawkins, TJ Senden, A Limaye, *X-ray tomography for mesoscale physics applications*, Physica A **339** pp152-158, 2004.
5. HK Tuy, *An inversion formula for cone-beam reconstruction*, Siam J. Appl. Math. **43** pp546-552, 1983.
6. LA Feldkamp, LC Davis, JW Kress, *Practical Cone-Beam Algorithm*, J. Opt. Soc. Am. A **1** pp612-619, 1984.
7. http://nf.apac.edu.au/facilities/sc/hardware.php
8. AP Sheppard, RM Sok, H Averdunk, *Techniques for image enhancement and segmentation of tomographic images of porous materials*, Physica A **339** 145-151, 2004
9. J Weickert, *Coherence-enhancing diffusion filtering*, Int. J. Comput. Vis. **31** pp111-127, 1999.
10. WK Pratt, *Digital Image Processing*, 2nd Edition, Wiley, New York, 1991.
11. V Caselles, R Kimmel, G Sapiro, *Geodesic active contours*, Int. J. Comput. Vis. **22** pp61-79, 1997.
12. L Vincent, P Soille, *Watersheds in digital spaces–an efficient algorithm based on immersion simulations*, IEEE Trans. Pattern Anal. Mach. Intell. **13** pp583-598, 1991.
13. JA Sethian, *Level Set Methods and Fast Marching Methods*, 2nd Edition, Cambridge University Press, 1999.
14. C Tropper, *Parallel and Distributed Discrete Event Simulation*, Nova Science Publishers, 2002.
15. CH Arns, MA Knackstedt, WV Pinczewski, KR Mecke, *Euler-Poincarè characteristics of classes of disordered media*, Phys. Rev. E **63** 03112, 2001.
16. WB Lindquist, AB Venkatarangan, JH Dunsmuir, TF Wong, *Pore and throat size distributions measured from synchrotron X-ray tomographic images of Fontainebleau sandstones*, J. Geophys. Research **105B** pp21508-21528, 2000.

17. WB Lindquist, *Quantitative analysis of three dimensional X-ray tomographic images*, in *Developments in X-ray Tomography III*, Ulrich Bonse, Editor, Proceedings of SPIE Vol. 4503, pp103-115, 2002.
18. M Hilpert, CT Miller, *Pore-morphology based simulation of drainage in totally wetting porous media*, Advances in Water Resources **24** pp243-255, 2001
19. J-F Thovert, F Yousefian, P Spanne, CG Jacquin, PM. Adler, *Grain reconstruction of porous media: Application to a low-porosity Fontainebleau sandstone*, Phys. Rev. E **63**, 061307, 2001
20. KR Brownstein, C Tarr, *Importance of classical diffusion in NMR studies of water in biological cells*, Phys. Rev. A **19** pp2446-2453, 1979.
21. CH Arns, MA Knackstedt, WV Pinczewski, WB Lindquist, *Accurate Computation of transport properties from microtomographic images*, Geophys. Res. Lett. **28** pp3361-3364, 2001
22. NS Martys, H Chen, *Simulation of multicomponent fluids in complex three-dimensional geometries by the lattice Boltzmann method* Physical Review E **53** pp743-750, 1996.
23. YH Qian, D D'Humieres, P Lamelland, *Lattice BGK models for Navier-Stokes equation*, Europhys. Lett. **2** pp291, 1986.
24. CH Arns, MA Knackstedt, WV Pinczewski, N Martys, *Accurate Computation of permeability from microtomographic images*, J. Petroleum Sci.and Eng., available online, 12 June 2004.
25. EJ Garboczi, AR Day, *An algorithm for calculating the effective linear elastic properties of heterogeneous materials: Three-dimensional results for composites with equal phase Poisson ratios*, Journal of the Mechanics and Physics of Solids **43** pp1349-62, 1995.
26. EJ Garboczi, *Finite element and finite difference programs for computing the linear electric and linear elastic properties of digital images of random materials.* Technical report, NIST Internal Report 6269. Available at http://ciks.cbt.nist.gov/monograph (Part II, Chapter 2), 1998.
27. CH Arns, *The influence of morphology on physical properties of reservoir rocks*, PhD thesis, University of New South Wales, 2002.
28. CH Arns, MA Knackstedt, WV Pinczewski, EG Garboczi, *Computation of linear elastic properties from microtomographic images: Methodology and agreement between theory and experiment*, Geophysics **67** pp1396-1405, 2002
29. FM Auzerias, J Dunsmuir, BB Ferreol, N Martys, J. Olson, TS Ramakrishnan, DH Rothman, LM Schwartz, *Transport in Sandstone: A study based on three dimensional microtomography*, Geophys. Res. Lett. **23** pp705-708, 1996
30. CH Arns, A Sakellariou, TJ Senden, AP Sheppard, RM Sok, WV Pinczewski, MA Knackstedt, *Petrophysical Properties Derived from X-Ray CT Images*, APPEA Journal **43** pp577-586, 2003.
31. CH Arns, A Sakellariou, TJ Senden, AP Sheppard, RM Sok, MA Knackstedt, WV Pinczewski, *Virtual Core Laboratory: Properties of reservoir rock derived from X-ray CT images*, SEG Expanded Abstracts Historical Series, pp1477-1480, 2003.
32. A Sakellariou, TJ Sawkins, TJ Senden, CH Arns, A Limaye, AP Sheppard, RM Sok, MA Knackstedt, WV Pinczewski, L Inge Berg, PE Øren, *Micro-CT facility for imaging reservoir rocks at pore scales*, SEG Expanded Abstracts Historical Series, pp1664-1667, 2003.
33. MA Knackstedt, CH Arns, A Limaye, A Sakellariou, TJ Senden, AP Sheppard, RM Sok, WV Pinczewski, GF Bunn, *Digital Core Laboratory: Properties of reservoir core derived from 3D images*, Society of Petroleum Engineers, 2004 Asia Pacific Conference on Integrated Modelling for Asset Management, Kuala Lumpur, **No. SPE 87009** March 2004.
34. CH Arns, H Averdunk, F Bauget, A Sakellariou, TJ Senden, AP Sheppard, RM Sok, WV Pinczewski, S Bakke, L Inge Berg, PE Øren, MA Knackstedt, *Pore Scale Characterisation of Carbonates using X-ray microtomography*, Society of Petroleum Engineers, 2004 Asia Pacific Conference on Integrated Modelling for Asset Management, Kuala Lumpur, **No. SPE 90368** March 2004.
35. CH Arns, H Averdunk, F Bauget, A Sakellariou, TJ Senden, AP Sheppard, RM Sok, WV Pinczewski, MA Knackstedt, *Digital Core Laboratory: Reservoir core analysis from 3D images*, American Rock Mechanics Association, Gulf Rocks 2004 - 6th North America Rock Mechanics Symposium (NARMS), Houston, Texas, **Paper 498**, June 2004.

36. CH Arns, H Averdunk, F Bauget, A Sakellariou, TJ Senden, AP Sheppard, RM Sok, WV Pinczewski, MA Knackstedt, *Digital Core Laboratory: Analysis of reservoir core fragments from 3D images*, 45th Annual Symposium SPWLA, Noordwijk, Netherlands, **Paper EEE**, June 2004.
37. P Ruegsegger, B Koller, R Müller, *A microtomographic system for nondestructive evaluation of bone architecture*, Calcif. Tissue Int. **58** pp24-29, 1996.
38. EL Ritman, SM Jorgensen, PE Lund, PJ Thomas, JH Dunsmuir, JC Romero, RT Turner, ME Bolander, *Synchrotron-based micro-ct of in situ biological basic functional units and their integration*, in *Proceedings of SPIE: Developments in X-Ray Tomography*, Ulrich Bonse, Editor, Proceedings of SPIE Vol. 3149, pp13-24, 1997.
39. JH Kinney, JT Ryaby, DL Haupt, NE Lane, *Three-dimensional in vivo morphometry of trabecular bone in the ovx rat model of osteoporosis*, Technol. Health Care **6** pp349-350, 1998.
40. S Nagaraja, TL Couse, RE Guldberg, *Trabecular bone microdamage and microstructural stresses under uniaxial compression*, Journal of Biomechanics, available online, 2 July 2004.
41. R Müller, P Ruegsegger, *Three dimensional finite element modelling of non-invasively assessed trabecular bone structures*, Med. Eng. Phys. **17** pp126-133, 1995.
42. R Müller, T Bösch, D Jarak, M Stauber, A Nazarian, M Tantillo, S Boyd, *Micro-mechanical evaluation of bone microstructures under load* in *Proceedings of SPIE: Developments in X-Ray Tomography III*, Ulrich Bonse, Editor, Proceedings of SPIE Vol. 4503, pp189-200, 2002.
43. AC Jones, AP Sheppard, RM Sok, CH Arns, A Limaye, H Averdunk, A Brandwood, A Sakellariou, TJ Senden, BK Milthorpe, MA Knackstedt, *Three-dimenional analysis of cortical bone structure using X-ray micro-computed tomography*, Physica A **339** pp125-130, 2004.
44. AC Jones, B Milthorpe, H Averdunk, A Limaye, TJ Senden, A Sakellariou, AP Sheppard, RM Sok, MA Knackstedt, A Brandwood, D Rohner, DW Hutmacher, *Analysis of 3D bone ingrowth into polymer scaffolds via micro-computed tomography imaging*, Biomaterials **25** pp4947-4954, 2004.
45. AC Jones, A Sakellariou, A Limaye, CH Arns, TJ Senden, TJ Sawkins, MA Knackstedt, D Rohner, DW Hutchmacher, A Brandwood and BK Milthorpe, *Investigation of bone microstructural features in regenerating bone using micro computed tomography*, Journal of Material Science: Materials in Medicine, **15** pp529-532, 2004.
46. M Saadatfar, MA Knackstedt, CH Arns, A Sakellariou, TJ Senden, AP Sheppard, RM Sok, H Steininger, W Schrof, *Polymeric foam properties derived from 3D images*, Physica A **339** pp131-136, 2004
47. J Duran, *Sands, Powders and Grains*, Springer-Verlag, 1999.
48. HM Jaeger, SR Nagel, *Physics of the Granular State*, Science **255** p1524, 1992.
49. S Torquato, *Random Heterogeneous Materials*, Springer-Verlag, New York, 2002.
50. T Aste, D Weaire, *The Pursuit of Perfect Packing*, Institute of Physics, Bristol, 2000.
51. P-G de Gennes, *Simple Views on Condensed Matter*, World Scientific, Singapore, 2003.
52. T Aste, M Saadatfar, A Sakellariou, TJ Senden, *Investigating the Geometrical Structure of Disordered Sphere Packings*, Physica A **339** pp16-23, 2004.
53. M Turner, A Sakellariou, CH Arns, TJ Senden, A Limaye, MA Knackstedt, *Towards modelling regolith permeability with high resolution X-ray tomography*, in *Advances in Regolith*, IC Roach, Editor, pp421-425, Canberra, October 2003.
54. ML Turner, L Knüfing, CH Arns, A Sakellariou, TJ Senden, AP Sheppard, RM Sok, A Limaye, WV Pinczewski, MA Knackstedt, *Three-dimensional imaging of multi-phase flow in porous media*, Physica A **339** pp166-172, 2004.
55. GD Yadav, FAL Dullien, I Chatzis, IF Macdonald, *Microscopic distribution of wetting and nonwetting phases in sandstones during immiscible displacements*, SPE Reservoir Eng. **137** 1987.
56. MJ Oak, *Three-phase relative permeability of water-wet berea*, in: SPE/DOE 7th Symposium on Enhanced Oil Recovery, 1990.
57. RJ Roberts, TJ Senden, MA Knackstedt, MB Lyne, *Spreading of Aqueous Liquids in Unsized Papers is by Film Flow*, J. Pulp Paper Sci. **29** pp123-131, 2003.
58. J Bico, D Quéré, *Precursors of impregnation*, Europhys. Letts. **61** pp348-353, 2003.
59. TJ Senden, MA Knackstedt, MB Lyne, *Droplet penetration into porous networks: Role of pore morphology*, Nordic Pulp and Paper Journal **15** pp554-563, 2000.